

1 **Regional inversion shows promise in capturing**
2 **extreme-event-driven CO₂ flux anomalies but is limited**
3 **by atmospheric CO₂ observational coverage**

4 **B. Byrne¹, J. Liu^{1,2}, K. W. Bowman^{1,3}, Y. Yin^{2,*}, J. Yun¹, G. D. Ferreira⁴,**
5 **S. M. Ogle^{4,5}, L. Baskaran¹, L. He⁶, X. Li⁷, J. Xiao⁸, K. J. Davis⁹**

6 ¹Jet Propulsion Laboratory, California Institute of Technology, Pasadena, CA, USA

7 ²Division of Geological and Planetary Sciences, California Institute of Technology, Pasadena, CA, USA

8 ³Joint Institute for Regional Earth System Science and Engineering, University of California, Los Angeles,
9 USA

10 ⁴Natural Resource Ecology Laboratory, Colorado State University, Fort Collins, CO 80523, United States
11 of America

12 ⁵Department of Ecosystem Science and Sustainability, Colorado State University, Fort Collins, CO 80523,
13 United States of America

14 ⁶Department of Global Ecology, Carnegie Institution for Science, Stanford, CA, United States of America

15 ⁷Research Institute of Agriculture and Life Sciences, Seoul National University, Seoul, South Korea

16 ⁸Earth Systems Research Center, Institute for the Study of Earth, Oceans, and Space, University of New
17 Hampshire, Durham, NH, USA

18 ⁹Department of Meteorology and Atmospheric Science, and Earth and Environmental Systems Institute,
19 The Pennsylvania State University, University Park, Pennsylvania

20 *Now at Department of Environmental Studies, New York University, New York, NY, USA

21 ©2023. All rights reserved. California Institute of Technology, government spon-
22 sorship acknowledged.

23 **Key Points:**

- 24 • Bottom-up and top-down methods independently capture reduced 2019 US Mid-
25 west carbon uptake
- 26 • Gaps in atmospheric CO₂ observations drive uncertainties in top-down estimates
- 27 • Nested inversion better localizes US Midwest Δ NEE relative to coarse global model

Corresponding author: Brendan Byrne, brendan.k.byrne@jpl.nasa.gov

Corresponding author: Junjie Liu, junjie.liu@jpl.nasa.gov

Abstract

Extreme climate events are becoming more frequent, with poorly understood implications for carbon sequestration by terrestrial ecosystems. A better understanding will critically depend on accurate and precise quantification of ecosystems responses to these events. Taking the 2019 US Midwest floods as a case study, we investigate current capabilities for tracking regional flux anomalies with “top-down” inversion analyses that assimilate atmospheric CO₂ observations. For this analysis, we develop a regionally nested version of the NASA Carbon Monitoring System-Flux (CMS-Flux) that allows high resolution atmospheric transport ($0.5^\circ \times 0.625^\circ$) over a North America domain. Relative to a 2018 baseline, we find US Midwest growing season net carbon uptake is reduced by 11-57 TgC (3–16%) for 2019 (inversion mean estimates across experiments). These estimates are found to be consistent with independent “bottom-up” estimates of carbon uptake based on vegetation remote sensing. We then investigate current limitations in tracking regional carbon emissions and removals by ecosystems using “top-down” methods. In a set of observing system simulation experiments, we show that the ability to recover regional carbon flux anomalies is still limited by observational coverage gaps for both in situ and satellite observations. Future space-based missions that allow for daily observational coverage across North America would largely mitigate these observational gaps, allowing for improved top-down estimates of ecosystem responses to extreme climate events.

Plain Language Summary

Extreme climate events, such as floods or heatwaves, can have major impacts on the carbon cycle. For example, widespread flooding in the US Midwest during 2019 delayed the planting of crops leading to reduced plant growth and carbon uptake relative to 2018. Here, we test how well this reduction in carbon uptake can be inferred from measurements of atmospheric CO₂. We find that these data can identify reduced net carbon uptake to the US Midwest during the 2019 floods, but that sparse observational coverage limits our ability to quantify the anomaly in net carbon uptake.

1 Introduction

Extreme events, including heat and precipitation extremes, are becoming more frequent (Shenoy et al., 2022; Q. Sun et al., 2021; Kirchmeier-Young & Zhang, 2020; Seneviratne et al., 2021). These events have significant implications for carbon sequestration in terrestrial ecosystems, often causing carbon losses in a single year equal to many years of carbon sequestration (Ciais et al., 2005; Byrne et al., 2021). This is concerning because Nature-based Climate Solutions (NbCSs), which aim to enhance the terrestrial carbon sink through improved land management, have been proposed as an important tool to mitigate CO₂ emissions (Fargione et al., 2018). The increasing frequency of extreme events may disrupt this process, creating a carbon-climate feedback where extreme-event-driven carbon emissions reduce the effectiveness of NbCSs (Zscheischler et al., 2018; Barkhordarian et al., 2021). Consequently, there is an urgent need to quantify the impact of extreme events on carbon uptake by ecosystems for policy programs and other climate applications.

“Top-down” methods offer an approach for estimating biosphere-atmosphere CO₂ fluxes based on observations of atmospheric CO₂. Typically, Bayesian inverse methods are used to estimate optimal surface fluxes based on constraints from prior information and atmospheric CO₂ observations. Although historically data limited, these techniques are increasingly used to quantify regional carbon cycle responses to extreme events, thanks to expansions of in situ CO₂ measurements and the introduction of space-based retrievals of column-averaged dry-air CO₂ mole fractions (X_{CO_2}) from missions like the Orbiting Carbon Observatory 2 (OCO-2) (Feldman et al., 2023; Byrne et al., 2021). Still, current

77 capabilities for tracking extreme events are not well understood. This study aims to im-
78 prove our characterization of these capabilities and identify current limitations.

79 As a case study, we examine the 2019 US Midwest floods. Intense precipitation dur-
80 ing that spring ($> 2\sigma$ above average) led to widespread flooding across the US Midwest,
81 a region that accounts for 40% of world corn and soybean production (Yin et al., 2020).
82 Inundation delayed crop planting by 2–3 weeks relative to 2018 across the region, with
83 an additional reduction of 6.8 million hectares in the total planted area. These factors
84 led to a 16-day shift in the seasonal cycle of photosynthesis relative to 2018, along with
85 a 15% lower peak value (Yin et al., 2020). In turn, crop yields across the US Midwest
86 were reduced by $\sim 14\%$, and a decrease in net carbon uptake of ~ 0.1 PgC was inferred
87 relative to the preceding years (Yin et al., 2020; Balashov et al., 2022). The relatively
88 simple (delayed planting) and well documented carbon cycle perturbation during this
89 event makes it an ideal case study for studying our ability to quantify carbon cycle per-
90 turbations using top-down and bottom-up methods.

91 To perform our analysis, we introduce a regionally nested version of the CMS-Flux
92 inversion system with high-resolution ($0.5^\circ \times 0.625^\circ$) atmospheric transport over North
93 America (see Sec. 2.1). This version offers advantages over the coarse-resolution ($4^\circ \times$
94 5°) global version of CMS-Flux. It reduces transport errors introduced by the coarsen-
95 ing of reanalysis winds (Stanevich et al., 2020; K. Yu et al., 2018) and better represents
96 assimilated CO_2 observations, resulting in improved localization of extreme-event-driven
97 CO_2 flux anomalies (Sec. 3.2.2).

98 The first objective of this study is to evaluate how well existing atmospheric ob-
99 serving systems can quantify flood-induced reductions in carbon uptake during 2019 rel-
100 ative to 2018. We conduct four inversions that assimilate (1) in situ CO_2 measurements
101 (IS), (2) OCO-2 land X_{CO_2} retrievals (LNLG), (2) both insitu and OCO-2 land data (LNL-
102 GIS), or (4) in situ, OCO-2 land and ocean data (LNLGOGIS)(Sec. 2.1). Climatolog-
103 ical prior fluxes are employed in each experiment, allowing us to attribute posterior anom-
104 alies in carbon uptake between years solely to the assimilation of atmospheric CO_2 data.
105 We then compare these estimates with an independent ensemble of remote-sensing bottom-
106 up estimates and with crop-yield data to assess their overall consistency (Sec. 3.1).

107 The second objective of this study is to assess the impact of existing observational
108 coverage gaps and the potential expansion of space-based X_{CO_2} measurements on our
109 ability to detect extreme-event-driven anomalies in CO_2 fluxes. To evaluate the effect
110 of expanded space-based observations, we devise a hypothetical observing system that
111 provides daily X_{CO_2} retrievals at 13:00 local time (similar to OCO-2). Subsequently, we
112 conduct observing system simulation experiments (OSSEs) for existing in situ data and
113 OCO-2 data as-well as the hypothetical observing system. For each OSSE, we evaluate
114 the effectiveness in capturing extreme-event-driven CO_2 flux anomalies (Sec. 3.2.1). Our
115 aim is to gain a deeper understanding of how observational coverage impacts our abil-
116 ity to quantify the influence of extreme events on CO_2 fluxes.

117 2 Methods

118 Sec. 2.1 introduces the configuration for the nested North America version of the
119 CMS-Flux atmospheric CO_2 inversion system, including its application for real data ex-
120 periments (Sec. 2.1.1) and OSSEs (Sec. 2.1.2). Sec. 2.2 describes remote-sensing bottom-
121 up NEE anomaly estimates used in this study. Sec. 2.3 describes the state crop produc-
122 tion estimates.

123

2.1 Top-down Δ NEE estimate

124

125

126

127

128

129

130

131

132

133

134

135

136

We establish a one-way nested inversion system covering the North America region, spanning from 40°W to 167.5°W and 14°N to 76°N . Within this domain, model transport is conducted at a spatial resolution of $0.5^{\circ} \times 0.625^{\circ}$ with a five-minute timestep, using archived MERRA-2 reanalysis data. We employ four-dimensional variational data assimilation (4D-Var) to optimize scaling factors on prior land and ocean fluxes. These fluxes are optimized at a coarser spatial and temporal resolution compared to the nested model transport. Spatially, a mask is applied to optimize fluxes over a $4^{\circ} \times 5^{\circ}$ grid, which is truncated at the land-ocean boundary. Temporally, we utilize a six-week inversion window and optimize weekly mean land and ocean scaling factors. The middle four weeks of the inversion window are retained as optimized fluxes, while the first and last weeks are excluded as spin-up and spin-down periods. We conduct a batch of eight six-week inversions offset by four weeks, yielding continuous fluxes from April 8th to November 18th for both 2018 and 2019, resulting in a total of 16 inversion runs.

137

138

139

140

141

142

143

144

145

146

147

148

149

150

151

152

153

154

155

156

For each experiment, the nested inversion setup is run three times using different prior fluxes (the BCs and ICs also differ for the real-data experiments, see Sec. 2.1.1). The prior NEE fluxes are derived from the posterior NEE fluxes of the GOSAT+surface+TCCON experiment by Byrne et al. (2020) and differ based on the employed prior NEE (CASA, SiB3, or FLUXCOM). A climatological seasonal cycle is calculated for each prior NEE flux over the period of 2010-2015. Subsequently, the climatological NEE seasonal cycle is partitioned into net primary production (NPP) and heterotrophic respiration (HR) components by subtracting the 2010-2015 mean seasonal cycle from the mean bottom-up NPP estimate (assumed to be 65% of mean GPP estimate here). In the inversions, we impose both the NPP and HR fluxes in the forward simulation, but optimize scaling factors only on the weekly mean HR fluxes. This choice is driven by the improved performance of this configuration during the spring and fall when NEE is close to zero, requiring large scaling factors to adjust the NEE flux. The posterior HR fluxes are not interpreted independently but combined with the prior NPP fluxes to obtain a posterior estimate of NEE for analysis. We generate prior uncertainties on the HR fluxes based on the full range of the three prior NEE fluxes. Prior ocean fluxes are derived similarly from the posterior ocean flux estimates of the GOSAT+surface+TCCON experiment by Byrne et al. (2020), and uncertainties on these estimates reflect the range among the three experiments that employ different NEE priors. The prior fluxes, posterior fluxes, and associated uncertainties are provided as supporting information.

157

158

159

160

161

162

163

164

165

166

167

168

169

170

In addition to the ocean, NPP, and HR fluxes, the forward simulations incorporate prescribed fossil fuel emissions, biomass burning emissions, biofuel emissions, and diurnal NEE. Fossil Fuel emissions used here were specifically made for the v10 OCO-2 modelling intercomparison project (MIP) (Byrne et al., 2023; Basu & Nassar, 2021). Biomass burning emissions are derived from the Global Fire Emissions Database version 4 (GFED4.1s) and scaled to incorporate diurnal variations in emissions (van der Werf et al., 2017). Biofuel emissions are obtained from the CASA-GFED4-FUEL dataset. Diurnal variations in NEE are based on the diurnal NEE variations from the CASA and SiB3 models, as described in Byrne et al. (2020). The SiB3 diurnal cycle is employed for the SiB3-based and FLUXCOM-based NEE priors, while the CASA diurnal cycle is prescribed for the CASA-based inversion. All of these fluxes are regridded from their native spatial resolution to $0.5^{\circ} \times 0.625^{\circ}$ (fossil fuel emissions were at $1.0^{\circ} \times 1.0^{\circ}$ degrees, biomass burning emissions were at $0.25^{\circ} \times 0.25^{\circ}$ degrees, and remaining fluxes were at $4^{\circ} \times 5^{\circ}$ as archived by Byrne et al. (2020)).

171

2.1.1 Real data experiment

172

173

First, we require atmospheric CO_2 boundary and initial conditions for the nested model. To generate these conditions, we conduct a global $4^{\circ} \times 5^{\circ}$ 4D-Var inversion that

174 optimizes scaling factors on prior land and ocean fluxes. These global inversions utilize
 175 the same configuration as Byrne et al. (2020). The resulting optimized global NEE and
 176 ocean fields are then employed in a $2^\circ \times 2.5^\circ$ global simulation to produce boundary con-
 177 ditions and initial conditions for the nested domain. The global inversions are performed
 178 three times, corresponding to each of the three prior NEE estimates. The nested inver-
 179 sion setup is subsequently executed three times using the three different prior fluxes, bound-
 180 ary conditions, and initial conditions based on the three distinct prior flux estimates.

181 Four sets of experiments are conducted, differing in the assimilated data. The “IS”
 182 experiment assimilates in situ CO_2 measurements from the global network of sites as de-
 183 scribed below. The “LNLG” experiment assimilates OCO-2 land data, including nadir
 184 and glint retrievals. The “LNLGIS” experiment assimilates both in situ and OCO-2 land
 185 data. Lastly, the “LNLGOGIS” experiment assimilates in situ, OCO-2 land data, and
 186 OCO-2 ocean glint retrievals.

187 In situ CO_2 measurements are obtained from version 8.0 of the NOAA GLOBALVIEW
 188 plus Obspack dataset (Schuldt et al., 2022). These data are provided on the X2019 CO_2
 189 scale but were back corrected to the X2007 CO_2 scale following Hall et al. (2021). We
 190 apply several filters to the in situ data before assimilation. Surface in situ CO_2 measure-
 191 ments are assimilated at their respective height above the surface, with inclusion crite-
 192 ria that the model surface elevation should differ by less than 500 m from the 15 arc-second
 193 ETOPO1 global elevation dataset (NOAA, 2021). Secondly, we only assimilate data with
 194 the CT_assim flag greater than or equal to one, which indicates data that is deemed as-
 195 similable for the NOAA CarbonTracker system. Finally, only measurements obtained
 196 between 11:00 and 17:00 local time are assimilated (when the atmospheric boundary layer
 197 is well mixed). The sites assimilated are: amt, bck, bmw, bra, brw, cba, cby, chl, cps,
 198 crv, egb, esp, est, etl, fsd, inu, inx, key, kum, lef, lew, llb, sct, sgp, uta, wbi, wgc, wkt,
 199 wsa. The sites with $\text{CT_assim} \geq 1$ that are not assimilated are: mbo, mex, mlo, mwo,
 200 nwr, omp, uts, wsd. We note that some sites with $\text{CT_assim} = 0$ may be assimilable, but
 201 more work is needed to characterize their suitability for assimilation. We apply the CT_MDM
 202 “model-data-mismatch” values as uncertainties on assimilated measurements. All air-
 203 craft data, including the ACT-America campaign data (Davis et al., 2021, 2018; Wei et
 204 al., 2021), are withheld for validation purposes. Monthly maps of data density are shown
 205 in Figure S1.

206 We employ X_{CO_2} retrieved using version 10 of NASA’s Atmospheric CO_2 Obser-
 207 vations from Space (ACOS) full-physics retrieval algorithm (O’Dell et al., 2018). Sub-
 208 sequently, OCO-2 “buddy” super-observations are calculated by averaging individual sound-
 209 ings into super-observations at a spatial resolution of $0.5^\circ \times 0.5^\circ$ within the same or-
 210 bit, assigning equal weights, following the approach by Liu et al. (2017). Monthly maps
 211 illustrating data density are shown in Figure S2.

212 The global inversions discussed in Sec. 3.2.2 follow an identical set-up as the nested
 213 inversions, with the same flux datasets regridded to $4^\circ \times 5^\circ$ globally.

214 **2.1.2 Observing System Simulation Experiments**

215 A series of OSSEs are conducted to explore the impact of observational coverage
 216 in quantifying carbon cycle perturbations resulting from extreme events. These OSSEs
 217 cover the same two year period as the real data inversions. Four OSSE experiments are
 218 carried out: IS, LNLG, LNLGOGIS, and one for a new hypothetical space-based observ-
 219 ing system that provides daily X_{CO_2} retrievals at 13:00 (1 pm). This hypothetical sys-
 220 tem, referred to as the ideal LEO mission, could comprise a dense constellation of low
 221 Earth orbit (LEO) sensors. The OSSEs are carried out following the same setup as the
 222 real data experiments, while the true atmospheric CO_2 boundary and initial conditions
 223 are implemented for the nested inversion.

224 For the ideal LEO mission, pseudo-observations are generated as follows: 1 pm ob-
 225 servations within each land $0.5^\circ \times 0.625^\circ$ grid cell are filtered to exclude instances of low-
 226 light conditions, cloudy conditions, and when the surface is covered by snow or ice. Frac-
 227 tional snow cover and cloud cover data are obtained from the MERRA-2 reanalysis dataset
 228 (Gelaro et al., 2017). Measurements are excluded for grid cells with a fractional area of
 229 land snow cover (FRSNO) greater than 75% and total cloud area fraction (ISCCPCLD-
 230 FRC) greater than 75% from the International Satellite Cloud Climatology Project (IS-
 231 CCP). Additionally, observations with an atmospheric path exceeding six air-masses are
 232 removed. We allow one super-obs within each gridcell per day. The uncertainty on the
 233 super-obs is defined to be 0.7 ppm, roughly matching OCO-2. Monthly maps of data den-
 234 sity for the ideal LEO mission are shown in Fig. S3.

235 True NEE fluxes for the OSSEs are generated by combining a climatological NEE
 236 seasonal cycle with anomalies from the bottom-up datasets. Climatological true NEE
 237 fluxes are obtained from the CASA-GFED3 model, which undergoes downscaling from
 238 monthly to three-hourly fluxes. These fluxes align with those described in Appendix 3
 239 of Byrne et al. (2020). Interannual variations in the true fluxes are introduced by incor-
 240 porating NEE anomalies taken to be 65% of the mean bottom-up GPP anomalies across
 241 the five datasets (see Sec. 2.2). Pseudo-observations are then generated by conducting
 242 a forward simulation using the nested model.

243 2.2 Remote-sensing bottom-up Δ GPP and Δ NEE estimates

244 We generate an ensemble of five bottom-up Δ GPP estimates by combining a num-
 245 ber of remote-sensing-based GPP datasets. Four of these are obtained from existing datasets:
 246 8 day FLUXCOM remote-sensing-based (RS) GPP (Jung et al., 2020), FluxSat Version
 247 2 (Joiner & Yoshida, 2020), GOSIF GPP (Li & Xiao, 2019), and the NIR_V-based GPP
 248 estimates of L. He et al. (2022). All of these data are regridded from their native res-
 249 olution to weekly temporal resolution and $0.5^\circ \times 0.625^\circ$ spatial resolution.

250 In addition, we estimate GPP directly from TROPOMI SIF data. This followed
 251 the same approach as Yin et al. (2020). Two GPP estimates are then calculated using
 252 land-cover-dependent SIF-to-GPP scaling factors from Li et al. (2018) and Y. Sun et al.
 253 (2017), which were adjusted by a factor of 0.64 to account for difference retrieval waveleg-
 254 nths between OCO-2 and TROPOMI (740 nm vs 757 nm). These factors were then ap-
 255 plied to gridded SIF data (0.08333° spatial and 8 day temporal resolution), while account-
 256 ing for the fractional vegetation cover within each gridcell. The GPP estimates were then
 257 regridded to $0.5^\circ \times 0.625^\circ$ spatial resolution. Any data gaps within the growing season
 258 are then filled by linear interpolation over time, while GPP is assumed to be zero for data
 259 gaps outside the growing season. Finally the two GPP estimates are averaged.

260 From these GPP datasets, we estimate an anomaly in NEE between 2018 and 2019
 261 by assuming the NEE anomaly is equal to the NPP anomaly, which is itself related to
 262 the GPP anomaly by:

$$\Delta\text{NEE} = -\Delta\text{NPP} = -0.60 \times \Delta\text{GPP} \quad (1)$$

263 The factor of 0.60 is an estimate of the carbon use efficiency (CUE), and is a relatively
 264 high estimate (Manzoni et al., 2018; Y. He et al., 2018), though may be representative
 265 of corn (S. Yu et al., 2023; Campioli et al., 2015). We assume an error of ± 0.1 in CUE,
 266 and perform error analysis using factors of 0.5 and 0.7. The conversion of ΔNPP to ΔNEE
 267 assumes that ΔHR is negligible. This is likely a poor assumption, but a limitation of remote-
 268 sensing estimates that are insensitive to HR variations. Previously, Yin et al. (2020) showed
 269 that bottom-up ΔNEE estimated assuming negligible ΔHR could reasonably reproduce
 270 observed atmospheric CO_2 enhancements during the 2019 US Midwest floods, provid-
 271 ing some evidence that ΔHR variations have a secondary impact.

272

2.3 State crop yields and NPP

273

274

275

276

277

Crop yields, which represents the amount of crop biomass removed from the field during harvest events, have been estimated using county-level crop yield data from the US Department of Agriculture (USDA) - National Agricultural Statistics Service (NASS) (USDA-NASS, 2020). The carbon content of crop yields was derived from the relationship:

$$Y_C = Y_{\text{NASS}} \times \text{DM} \times C_f, \quad (2)$$

278

279

280

281

where Y_C is the crop yield, in units of carbon, Y_{NASS} is the annual county-level crop yield data from USDA-NASS, DM is the dry matter content for each crop, and C_f is carbon content crop factor. Crop NPP (NPP_{crop}), representing the net carbon uptake by crops, was derived from the crop yield estimates using the following equation:

$$\text{NPP}_{\text{crop}} = Y_{\text{NASS}} \times \frac{1}{\text{HI}} \times (1 + \text{RRS}) \times \text{DM} \times C_f, \quad (3)$$

282

283

284

285

286

287

288

289

290

291

292

where HI is the harvest index for each crop, i.e., the proportion of harvested material (e.g., grains) in relation to total crop aboveground biomass; and RRS is the root:shoot ratio for each crop. We used crop-specific factors for dry matter, root:shoot ratios, harvest indices, and carbon content following the methods in West et al. (2010, 2011) and Ogle et al. (2015). Crop yields and NPP were estimated for over 20 crops, which together represented >99% of total US crop production (USDA-NASS, 2020). Uncertainty in estimates were propagated through a Monte Carlo approach with 10,000 replicates and probability distribution functions for all input data and factors. The results are based on the mean and 95% confidence intervals from the final distribution of simulated values. We note that NASS only included uncertainty in crop yield data for 2020 so we assumed a similar level of uncertainty in crop yields for the other years.

293

3 Results

294

3.1 Flood-induced NEE anomalies

295

296

297

298

299

300

301

302

303

304

305

306

307

308

Figure 1a–b illustrates the difference in June–July NEE between 2019 and 2018 ($\Delta\text{NEE} = \text{NEE}_{2019} - \text{NEE}_{2018}$) for both the remote-sensing bottom-up (ensemble mean) and top-down (LNLGOGIS) estimates. The analyses reveal a significant decrease in CO_2 uptake (positive ΔNEE) specifically in the US Midwest region. This pronounced positive ΔNEE signal in the US Midwest stands out compared to the rest of the continent. Figure 1c presents the 5 week running mean time series of ΔNEE over the US Midwest. Both the top-down and bottom-up estimates depict a positive ΔNEE signal throughout Jun–Jul, with the anomaly peaking towards the end of June. However, during Aug–Sep, the top-down and bottom-up estimates suggest a negative ΔNEE in the US Midwest. Across the rest of the continent (Figure 1d), anomalies are weaker. The top-down estimate suggests a positive anomaly outside the US Midwest during August, while the bottom-up estimate suggests no significant anomalies. The supplementary materials display the maps and timeseries for the other top-down experiments (Fig. S4) and individual bottom-up datasets (Fig. S5).

309

310

311

312

313

314

315

316

317

318

319

Figure 2 shows US Midwest ΔNEE for each of the top-down and bottom-up estimates. In addition, an estimate of the anomaly in net primary production for crops ($\Delta\text{NPP}_{\text{crop}}$) derived from crop yield data is shown. All estimates suggest positive ΔNEE over the study period (-6–85 TgC for top-down, 15–78 TgC for bottom-up, and 36–65 TgC for yield-based estimates). We find that June–July ΔNEE drives the annual anomaly with uptake reduced by 24–76 TgC in top-down estimates and 38–131 TgC in bottom-up estimates. The bottom-up estimates suggest this is moderated when integrating across the growing season due to greater carbon uptake during Aug–Sep (-56 TgC to -15 TgC), while the top-down estimates are less consistent during Aug–Sep, ranging from -37 TgC to 34 TgC. Figure S6 demonstrates that the bottom-up and top-down ΔNEE generally show similar June–July ΔNEE across the CONUS Climate Assessment Regions. In particular, we

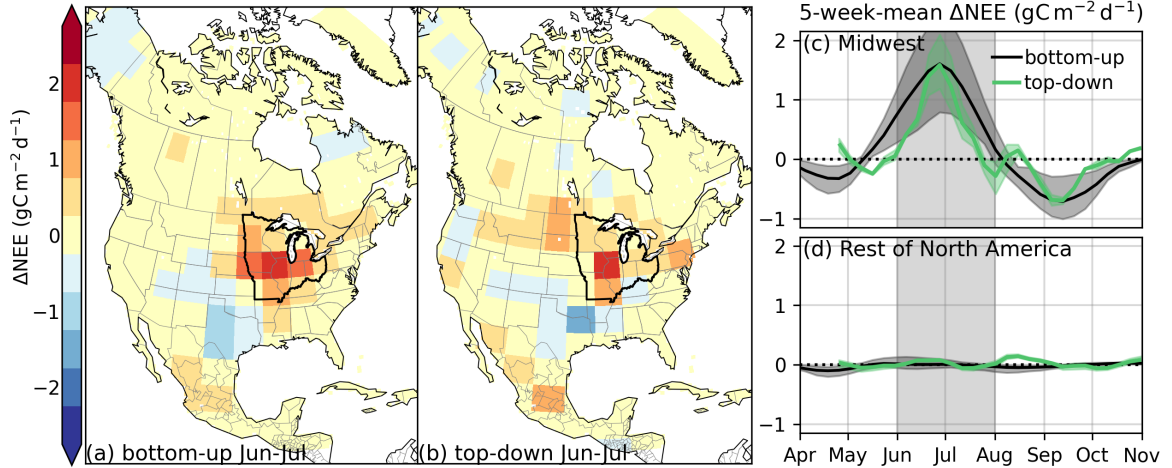


Figure 1. (a) Bottom-up and (b) top-down (LNLGOGIS) spatial patterns of June–July mean ΔNEE ($\text{NEE}_{2019} - \text{NEE}_{2018}$) at $4^\circ \times 5^\circ$ spatial resolution. (c) US Midwest and (d) rest of North America 5-week-mean ΔNEE . The US Midwest is defined as the area within Illinois, Indiana, Iowa, Michigan, Minnesota, Missouri, Ohio, and Wisconsin and is indicated by the black outline in panels (a) and (b). The shading shows the range around the mean estimate for the inversions using three different priors and for the five bottom-up GPP datasets.

320 find that all estimates obtain negative ΔNEE across the Southern Great Plains (-22 to
 321 -46 TgC), resulting from the 2018 drought (Turner et al., 2021).

322 These findings suggest that both in situ and OCO-2 data provide adequate obser-
 323 vational coverage to detect the June–July ΔNEE signal resulting from the 2019 US Mid-
 324 west floods. However, some differences are also evident. The experiments disagree in the
 325 sign of Aug–Sep ΔNEE . The IS experiment shows negative Aug–Sep ΔNEE that largely
 326 compensates for the positive June–July ΔNEE . Conversely, the LNLG experiment gives
 327 positive Aug–Sep ΔNEE but the smallest June–July ΔNEE . There are some spatial dif-
 328 ferences as-well, for example, the IS experiment suggests larger positive ΔNEE in west-
 329 ern Canada and negative ΔNEE in the southeast during Jun–Jul than the other experi-
 330 ments (Fig. S4). The LNLGIS and LNLGOGIS experiments yield quite similar results.
 331 The relative accuracy of these different estimates is challenging to evaluate, as a num-
 332 ber of different drivers could contribute to differences but all experiments exhibit good
 333 agreement with independent aircraft CO_2 measurements during 2018 and 2019 (Text S1,
 334 Fig. S7–S12). The disparities between experiments may arise from differences in obser-
 335 vational coverage and this hypothesis is examined in Sec. 3.2.1.

336 The bottom-up estimates show some notable differences in the magnitude of ΔNEE
 337 over the US Midwest and the spatial structure of ΔNEE outside the US Midwest (Fig. S5).
 338 FLUXCOM consistently displays the weakest ΔNEE signal, and has been previously shown
 339 to underestimate interannual variations in NEE and GPP (Jung et al., 2020). Outside
 340 the US Midwest, the NIR_V-based estimate shows negative values across the western half
 341 of North America, which are not observed in any other estimates, while the TROPOMI-
 342 based estimate indicates positive ΔNEE across a large portion of eastern Canada. Con-
 343 sequently, the net June–July ΔNEE signal outside the US Midwest varies across datasets,
 344 ranging from -218 TgC to 187 TgC.

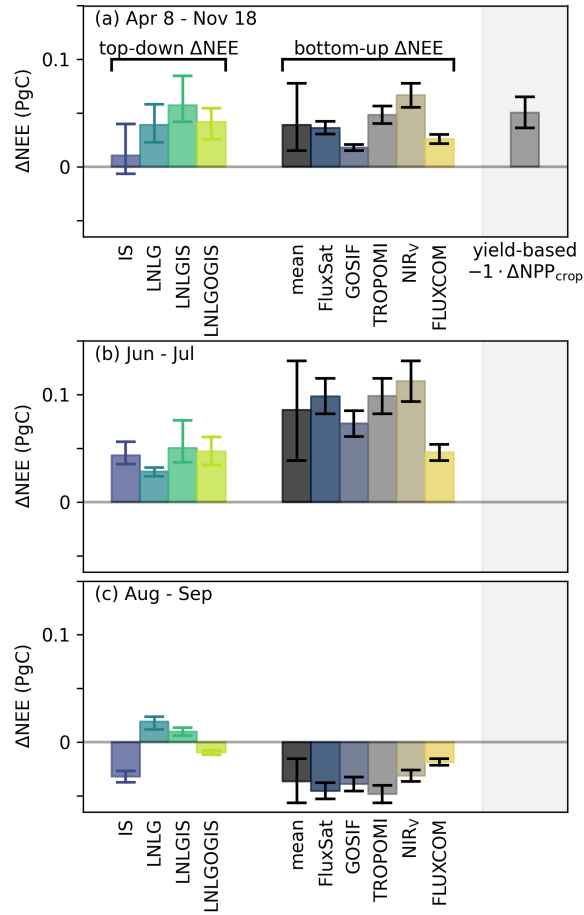


Figure 2. Top-down ΔNEE , bottom-up ΔNEE , and yield-based ΔNPP for crops ($\Delta\text{NPP}_{\text{crop}}$) over the US Midwest. ΔNEE is calculated for (a) the entire inversion period (April 8th – Nov 18th), (b) June–July and (c) Aug–Sep. The top-down estimates show the mean and range obtained using three different priors. Uncertainty bars for the top-down estimates show the range using three priors, while the uncertainties on the bottom-up show the range of using carbon use efficiencies of 0.5–0.7.

345

3.2 Sensitivity experiments

346

3.2.1 Impact of observational coverage

347

348

349

350

351

352

Although both the in situ network and OCO-2 were able to identify a positive US Midwest ΔNEE signal, we found substantial differences between the top-down experiments. Here we perform OSSEs to investigate whether gaps in observational coverage could explain these differences. Further, we test whether increased observational coverage (in an ideal LEO constellation) would substantially improve top-down estimates of extreme-event-driven carbon cycle perturbations.

353

354

355

356

357

358

359

360

361

362

363

Figure 3 shows the true and posterior ΔNEE for the OSSEs. All OSSEs recover positive ΔNEE to the US Midwest, consistent with the real data experiments. However, June–July US Midwest ΔNEE is underestimated by 43% for IS, 75% for LNLG, 48% for LNLGOGIS and 15% for the ideal LEO constellation. In addition, the inversions tend to introduce a positive June–July ΔNEE outside the US Midwest that is not present in the truth. Over June–July, the true continental-scale ΔNEE is 89 TgC, while the mean inversion estimates are 163 TgC (error of +74 TgC) for IS, 93 TgC (error of +4 TgC) for LNLG, 68 TgC (error of -21 TgC) for LNLGOGIS, and 93 TgC (error of +4 TgC) for ideal LEO. A similar large continental-scale positive June–July ΔNEE was found for the real data IS experiment (Fig. S4ci). One possible explanation is that the limited spatial coverage of the in situ (Fig. S1) data may limit the ability to capture aggregate continental-scale budgets using a one-way nested system.

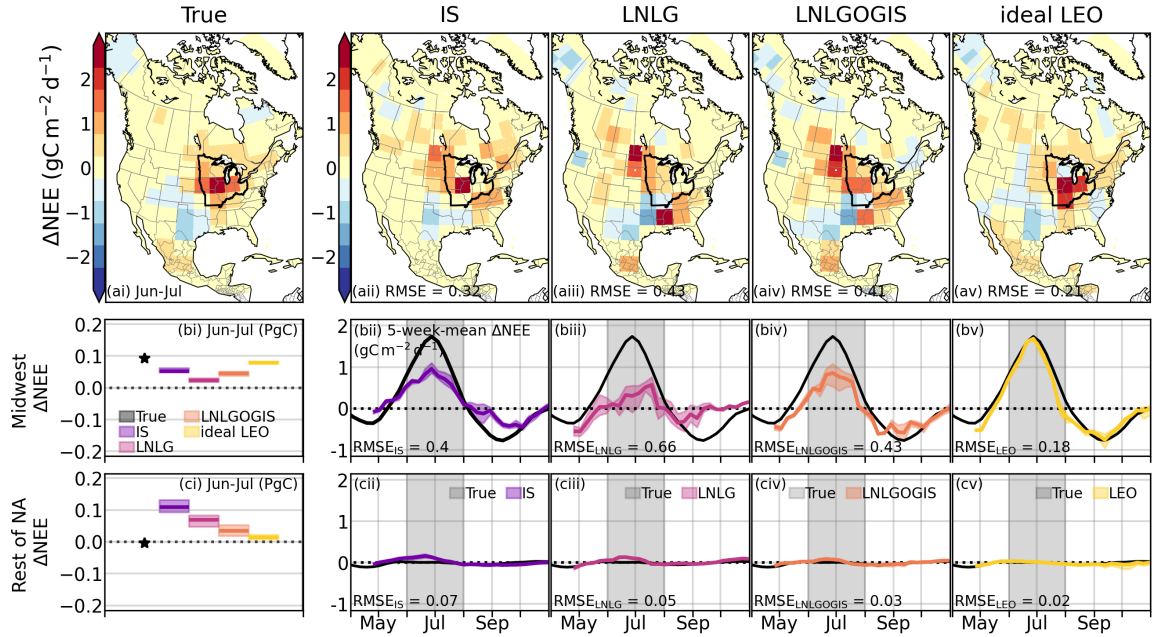


Figure 3. ΔNEE estimates for the OSSEs. Panel (ai) shows the true June–July ΔNEE maps, while panels (aai)–(av) show the OSSE posterior June–July ΔNEE maps and RMSE across grid-cells ($\text{gC m}^{-2} \text{d}^{-1}$). The net US Midwest Jun–Jul ΔNEE (PgC) is shown for each OSSE in panel (bi), and the timeseries of 5-week-mean ΔNEE is shown for each experiment in panels (bii)–(bv), with RMSE across weeks ($\text{gC m}^{-2} \text{d}^{-1}$). The same quantities are shown for the rest of North America in panels (ci)–(cv).

364

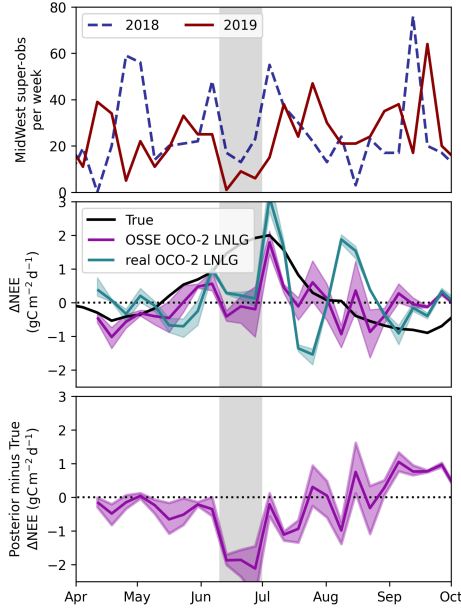


Figure 4. Weekly timeseries of (top) number of OCO-2 super-obs in the US Midwest for 2018 and 2019. (middle) Weekly Δ NEE in the US Midwest for the truth, OCO-2 OSSE and real OCO-2 LNLG experiment. (bottom) Difference between posterior and true Δ NEE for the OCO-2 OSSE. The shading shows the range around the mean estimate for the inversions using three different priors.

365 Overall, the LNLG OSSE shows the worst performance at isolating the US Mid-
 366 west Δ NEE. We suggest that this could be related to interannual variations in the ob-
 367 servational coverage. Figure 4a shows that the number of LNLG weekly samplings over
 368 the US Midwest can be quite variable from year to year. In particular, there are only
 369 16 super-obs in the US Midwest during the three week period of June 11, 2019 to July
 370 2 2019. This coincides with near zero Δ NEE for both the real data LNLG inversion and
 371 OSSE (Fig. 4b), and the period with the largest error in Δ NEE for the OSSE (Fig. 4c).
 372 These results suggest that data gaps in OCO-2, particularly differences in observational
 373 coverage between years, limit our ability to estimate inter-annual variations in NEE at
 374 high spatio-temporal resolution.

375 The increased sampling from combining the datasets (LNLGOGIS) appears to mod-
 376 erately improve performance, particularly in isolating June–July Δ NEE to the US Mid-
 377 west (relative to LNLG) and better capturing the continental-scale Δ NEE (relative to
 378 IS). However, the ideal LEO constellation results in much improved performance in both
 379 space and time. The ideal LEO constellation reduces June–July RMSE across $4^\circ \times 5^\circ$
 380 regions by 34–51% and the 5-week-mean Δ NEE US Midwest RMSE by 55–73%. This
 381 comparison suggests that top-down estimates of extreme-event-driven perturbations to
 382 carbon uptake remain observationally-limited and that expanded space-based observ-
 383 ing systems will improve these estimates.

3.2.2 Comparison between nested and global inversions

384
 385 The nested CMS-Flux inversion system in this study offers both advantages and
 386 disadvantages compared to a global CMS-Flux inversion system. One major advantage
 387 is the ability to run transport at a higher resolution ($0.5^\circ \times 0.625^\circ$) compared to the global

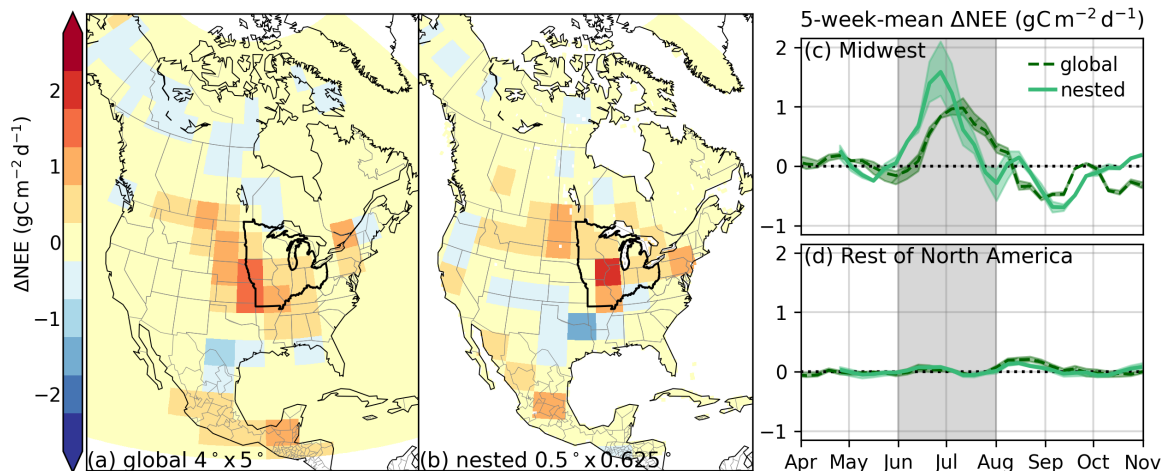


Figure 5. Comparison of the global $4^\circ \times 5^\circ$ and nested inversion results. Maps of June–July ΔNEE from the LNLGOGIS experiment are shown for (a) the global $4^\circ \times 5^\circ$ inversion and (b) the nested inversion. Weekly ΔNEE in the US Midwest after applying a 5-week running mean are also show for (c) the US Midwest and (d) rest of North America.

388 system ($4^\circ \times 5^\circ$). This higher resolution enables tracer transport to be closer to the par-
 389 ent model, as spatial averaging of meteorological fields can average out eddy transport,
 390 particularly affecting vertical motions (Stanevich et al., 2020). Additionally, a higher res-
 391 olution model grid reduces representativeness errors, allowing better representation of
 392 fine-scale features that influence observations, such as topography. The primary disad-
 393 vantage of the one-way nested system used in this study is the assumption of perfect bound-
 394 ary conditions and the inability to assimilate atmospheric CO_2 observations outside the
 395 nested domain. In a global inversion, fluxes over North America would impact measure-
 396 ments downwind, providing a powerful constraint on large-scale fluxes, including the net
 397 North American flux (Liu et al., 2015). A bias in flux at the continental scale would af-
 398 fect CO_2 fields across the entire Northern Hemisphere. Since the nested inversion lacks
 399 this constraint, significant errors in continental-scale fluxes may go undetected. Further-
 400 more, biases in the imposed boundary CO_2 fields can propagate into optimized fluxes.

401 In order to assess the performance of the one-way nested inversion, we compare the
 402 obtained ΔNEE with the global version of CMS-Flux using the same inversion config-
 403 uration, whenever possible. Figure 5 presents the results for both the global and nested
 404 versions of CMS-Flux. It is observed that the nested version of CMS-Flux effectively iso-
 405 lates ΔNEE to the US Midwest region during June–July. In contrast, the global model
 406 exhibits spatially broader positive ΔNEE across the US Midwest and Great Plains, re-
 407 sulting in a significantly reduced ΔNEE estimate for the US Midwest during June–July.
 408 The spatial pattern of ΔNEE for the nested model aligns more closely with the bottom-
 409 up estimate, suggesting that this system better captures the overall event. This indicates
 410 that, considering the observational coverage provided by LNLGOGIS, the benefits of re-
 411 duced transport and representativeness errors in the nested model outweigh the detri-
 412 mental impact of a limited domain.

413 We note that achieving good performance with nested version of CMS-Flux was
 414 challenging, and required a number of trial-and-error inversions. This included varying
 415 the size of the state vector spatially ($0.5^\circ \times 0.625^\circ$ versus $4^\circ \times 5^\circ$ grid) and temporally
 416 (weekly, bi-weekly, monthly intervals). It also involved adjusting the prior constraints
 417 (optimizing HR rather than NEE, adjusting prior uncertainties). We suggest that these

418 challenges are due to greater regularization requirements for the nested model in com-
 419 parison to the global model. The sensitivities of observations to surface fluxes are lim-
 420 ited to 1–2 weeks by the one-way nesting, such that large-scale constraints are imposed
 421 by the boundary conditions (Feng, Lauvaux, Davis, et al., 2019; Feng, Lauvaux, Keller,
 422 et al., 2019). Thus, the flux signal in the domain is generally much smaller than for the
 423 global model, where downwind observations provide important information for upwind
 424 continental-scale regions (Liu et al., 2015). We suggest that imposing an error correla-
 425 tion length between state-vector elements may be an effective approach for regulariza-
 426 tion in a nested inversion context (see Sec. 4.1), however, this is beyond the scope of our
 427 current study.

428 4 Discussion and Conclusions

429 Both top-down and bottom-up approaches capture a flood-induced reduction in net
 430 carbon uptake during the 2019 US Midwest floods. The top-down approach gave mean
 431 estimates of 11 TgC (IS), 39 TgC (LNLG), 57 TgC (LNLGIS), 42 TgC (LNLGOGIS)
 432 for US Midwest growing season Δ NEE. Meanwhile, the bottom-up datasets gave a mean
 433 estimate of 39 TgC (range: 15–78 TgC). These magnitudes are significant compared to
 434 anthropogenic emissions, amounting to as much as 28% of the US Midwest’s annual fos-
 435 sil fuel emissions (300 TgC yr⁻¹ for 2019, U.S. Energy Information Administration (2023)).
 436 In addition, this anomaly is comparable to the year-to-year variations in fossil fuel emis-
 437 sions (SD: 25 TgC yr⁻¹), even including the reduction of regional emissions by 36 TgC yr⁻¹
 438 due to COVID-19 lockdowns in 2020.

439 In the context of more frequent heat and precipitation extremes (Seneviratne et
 440 al., 2021), accurate estimates of the carbon cycle responses will be critical for monitor-
 441 ing carbon budgets and evaluating carbon-climate feedbacks. The results of this study
 442 show that both top-down and bottom-up approaches demonstrate skill in capturing Δ NEE
 443 resulting from the 2019 Midwest floods, however a number of deficiencies were also iden-
 444 tified. In the following sub-sections, we highlight current challenges and opportunities
 445 in quantifying carbon cycle extremes.

446 4.1 Top-down

447 Observational gaps in atmospheric CO₂ observations are identified as a key lim-
 448 itation in applying top-down methods to quantify extreme-event-driven Δ NEE, consis-
 449 tent with recent studies of the European carbon budget (W. He et al., 2023; Munassar
 450 et al., 2022; Monteil et al., 2020; Thompson et al., 2020). Through a series of OSSE ex-
 451 periments, it was demonstrated that gaps in both the in situ network and OCO-2 sam-
 452 pling impact the accuracy of Δ NEE estimates. While assimilating these two datasets con-
 453 currently partially mitigates the issue, fully resolving the problem requires expanded ob-
 454 servations. Coverage similar to the ideal LEO observing system could be developed by
 455 combining multiple individual satellites, and motivates future studies that assimilate X_{CO₂}
 456 retrievals from multiple space-based observing systems concurrently (e.g., GOSAT, OCO-
 457 2, and OCO-3). In addition, efforts should be made to ensure consistency in X_{CO₂} re-
 458 trievals between existing and planned missions (e.g., CO2M, GOSAT-GW). Expanding
 459 the in situ network would also likely enhance the ability to capture regional flux anom-
 460 alies more effectively, however, this was not specifically explored.

461 Although current observing gaps are found to be a major limitation, there may be
 462 approaches to better regularize the inverse problem and reduce the impact of these gaps.
 463 In particular, applying off-diagonal co-variances in the prior error covariance matrix could
 464 be employed to adjust fluxes where observations are missing (Chen et al., 2023). Apply-
 465 ing spatial co-variances will likely be especially important for in situ inversions, while
 466 applying temporal co-variances may be most useful for OCO-2 X_{CO₂} inversions. Of course,
 467 such an approach will only improve flux estimates if spatial and temporal co-variances

468 are truly present, such that this approach will be limited by a correlation length scale.
 469 In addition, imposing realistic prior IAV could also be a fruitful approach, as has been
 470 done in previous studies evaluating the 2019 US Midwest floods (Yin et al., 2020; Bal-
 471 ashov et al., 2022). However, high-confidence is needed in imposed prior IAV, as inac-
 472 curate prior IAV can significantly degrade posterior IAV estimates (Byrne et al., 2019).
 473 Text S2 and Figs. S13-15 show that imposing bottom-up IAV in the prior results in larger
 474 posterior Δ NEE anomalies during the Midwest Floods for all experiments. This is con-
 475 sistent with the Δ NEE anomalies being underestimated when using climatological pri-
 476 ors, as was found in the OSSEs.

477 Finally, this study investigated the utility of a one-way nested version of CMS-Flux
 478 with $0.5^\circ \times 0.625^\circ$ spatial resolution relative to the global model at $4^\circ \times 5^\circ$ degree spa-
 479 tial resolution. We note that developing a nested inversion system involved considerable
 480 effort in tuning the state vector structure, assimilation window, and prior constraints.
 481 Nevertheless, we found that the nested model better allocated flood-induced Δ NEE to
 482 the US Midwest, suggesting that the improved model transport and observation repre-
 483 sentation of the nested model improved the overall performance relative to the global
 484 model, consistent with several recent studies (Monteil et al., 2020; Hu et al., 2019). How-
 485 ever, the nested model has some disadvantages, especially the inability to assimilate down-
 486 wind observations outside the model domain that may limit the utility of the nested model
 487 in other applications. Transport uncertainty and boundary condition errors may lead to
 488 significant challenges for nested inversions (Munassar et al., 2023; Kim et al., 2021; Chen
 489 et al., 2019; Lauvaux et al., 2012), but were not obvious in our analyses. We note that
 490 high-resolution models will be needed to take advantage of upcoming wide-swath sam-
 491 pling missions, such as CO2M (~ 250 km swath) or GOSAT-GW (~ 400 km swath).

492 4.2 Bottom-up

493 Remote-sensing-based bottom-up estimates of Δ NEE provided a consistent picture
 494 of reduced net uptake during the 2019 Midwest floods but differed significantly in mag-
 495 nitude. The primary source of this variability stems from translating space-based reflectance
 496 or SIF observations to GPP, leading to a range in Δ GPP between datasets of 120% of
 497 the mean. Indeed, estimating the magnitude of GPP from remote sensing datasets is chal-
 498 lenging due to satellite signals that could be influenced by factors such as cloud cover-
 499 age and soil background, in addition to calibration that is predominantly relying on bench-
 500 marks provided by eddy covariance sites. We encourage research into approaches that
 501 can reduce uncertainties on large-scale GPP magnitudes, possibly through top-down con-
 502 straints from Carbonyl Sulphide.

503 Additional uncertainties were introduced in estimating Δ NEE from Δ GPP. Due
 504 to the inherent limitations of remote sensing, which can track GPP but not the total ecosys-
 505 tem respiration (the sum of HR and AR), certain assumptions must be made. First, to
 506 estimate AR, we assumed that Δ GPP and Δ NPP can be related through a constant car-
 507 bon use efficiency (CUE) parameter that varies across vegetation type, age, and man-
 508 agement practices (Campioli et al., 2015; DeLucia et al., 2007; Manzoni et al., 2018; Y. He
 509 et al., 2018; S. Yu et al., 2023). In our analysis, we adopted a mean value of 0.60 with
 510 an uncertainty of range 20% (0.5–0.7), which encompasses most literature estimates. Sec-
 511 ond, we assumed that the influence of Δ HR on the Δ NEE was negligible. The secondary
 512 impact of Δ HR is supported by Yin et al. (2020), who were able to reasonably repro-
 513 duce observed atmospheric CO₂ enhancements during the 2019 US Midwest floods while
 514 neglecting Δ HR variations. Still, it is important to note that HR is sensitive to varia-
 515 tions in temperature and moisture. Terrestrial biosphere models could serve as poten-
 516 tial tools for estimating Δ HR (e.g., Balashov et al. (2022)) as remote sensing does not
 517 adequately capture variations in HR, which is significantly influenced by the availabil-
 518 ity of labile carbon. However, the accuracy of these model-driven estimates remains chal-
 519 lenging to verify.

5 Open Research

Once accepted for publication, the prior and posterior fluxes, TROPOMI-based GPP, and NIR_V-based GPP will be archived with a DOI. During the review processes the data are available by contacting Brendan Byrne. The atmospheric CO₂ inversion analyses performed in this study used the CMS-Flux model, which is based on the GEOS-Chem Adjoint model that can be accessed from the GEOS-Chem Wiki (<https://wiki.seas.harvard.edu/geos-chem>). OCO-2 X_{CO₂} Lite files can be downloaded from the GES DISC (<https://disc.gsfc.nasa.gov>). In Situ CO₂ measurements (Schuldt et al., 2022) can be downloaded from <https://gml.noaa.gov/ccgg/obspace/>. GFED biomass burning emissions (van der Werf et al., 2017) were downloaded from <https://globalfiredata.org/>. Fossil fuel emissions (Basu & Nassar, 2021) were downloaded from <https://doi.org/10.5281/zenodo.4776925>. MERRA-2 reanalysis data (Gelaro et al., 2017) was downloaded from <https://disc.gsfc.nasa.gov/>. TROPOMI SIF data are accessed online at <https://data.caltech.edu/records/1347> (DOI: 10.22002/D1.1347). FluxSat Version 2 (Joiner & Yoshida, 2021) were downloaded from the ORNL DAAC (<https://daac.ornl.gov>). GOSIF GPP (Li & Xiao, 2019) were downloaded from <http://data.globalecology.unh.edu/>. FLUXCOM GPP (Jung et al., 2020) was downloaded from the aata portal of the Max Planck Institute for Biogeochemistry (<https://www.bgc-jena.mpg.de/geodb/projects/Home.php>).

Acknowledgments

The research carried out at the Jet Propulsion Laboratory, California Institute of Technology, was under a contract with the National Aeronautics and Space Administration. Funding for the research was from the NASA CMS (grant nos. 80NSSC21K1060, 80NM0018F0583) and OCO science team (grant np. 80NM0018F0583) programs. Resources supporting this work were provided by the NASA High-End Computing (HEC) program through the NASA Advanced Supercomputing (NAS) Division at Ames Research Center.

References

- Balashov, N., Ott, L. E., Weir, B., Basu, S., Davis, K. J., Miles, N. L., . . . Stauffer, R. M. (2022). Flood impacts on net ecosystem exchange in the midwestern and southern united states in 2019. doi: 10.1002/essoar.10512359.1
- Barkhordarian, A., Bowman, K. W., Cressie, N., Jewell, J., & Liu, J. (2021). Emergent constraints on tropical atmospheric aridity—carbon feedbacks and the future of carbon sequestration. *Environmental Research Letters*, 16(11), 114008.
- Basu, S., & Nassar, R. (2021, January). *Fossil Fuel CO Emissions for the OCO2 Model Intercomparison Project (MIP)*. Zenodo. Retrieved from <https://doi.org/10.5281/zenodo.4776925> (Previous versions available from (2018): <https://gmao.gsfc.nasa.gov/gmaoftp/sourish/ODIAC/2018/distrib/>, (2017): <ftp://aftp.cmdl.noaa.gov/data/ccgg/ODIAC/2017/distrib/>, (2016): <ftp://aftp.cmdl.noaa.gov/data/ccgg/ODIAC/2016/distrib/>, (2015a): <ftp://aftp.cmdl.noaa.gov/data/ccgg/ODIAC/2015a/distrib/>) doi: 10.5281/zenodo.4776925
- Byrne, B., Baker, D. F., Basu, S., Bertolacci, M., Bowman, K. W., Carroll, D., . . . Zeng, N. (2023). National CO₂ budgets (2015–2020) inferred from atmospheric CO₂ observations in support of the global stocktake. *Earth System Science Data*, 15(2), 963–1004. Retrieved from <https://essd.copernicus.org/articles/15/963/2023/> doi: 10.5194/essd-15-963-2023
- Byrne, B., Jones, D. B. A., Strong, K., Polavarapu, S. M., Harper, A. B., Baker, D. F., & Maksyutov, S. (2019). On what scales can gosat flux inversions constrain anomalies in terrestrial ecosystems? *Atmos. Chem. Phys.*, 19(20), 13017–13035. Retrieved from <https://www.atmos-chem-phys.net/19/13017/2019/> doi: 10.5194/acp-19-13017-2019

- 571 Byrne, B., Liu, J., Lee, M., Baker, I. T., Bowman, K. W., Deutscher, N. M., ...
 572 Wunch, D. (2020). Improved constraints on northern extratropical CO₂
 573 fluxes obtained by combining surface-based and space-based atmospheric CO₂
 574 measurements. *Journal of Geophysical Research: Atmospheres*, *125*. doi:
 575 10.1029/2019JD032029
- 576 Byrne, B., Liu, J., Lee, M., Yin, Y., Bowman, K. W., Miyazaki, K., ... Paton-
 577 Walsh, C. (2021). The carbon cycle of southeast Australia during 2019–2020:
 578 Drought, fires, and subsequent recovery. *AGU Advances*, *2*(4), e2021AV000469.
 579 doi: 10.1029/2021AV000469
- 580 Campioli, M., Vicca, S., Luyssaert, S., Bilcke, J., Ceschia, E., Chapin III, F. S., ...
 581 others (2015). Biomass production efficiency controlled by management in
 582 temperate and boreal ecosystems. *Nature geoscience*, *8*(11), 843–846.
- 583 Chen, H. W., Zhang, F., Lauvaux, T., Davis, K. J., Feng, S., Butler, M. P., & Alley,
 584 R. B. (2019). Characterization of regional-scale CO₂ transport uncertainties
 585 in an ensemble with flow-dependent transport errors. *Geophysical Research*
 586 *Letters*, *46*(7), 4049–4058.
- 587 Chen, H. W., Zhang, F., Lauvaux, T., Scholze, M., Davis, K. J., & Alley, R. B.
 588 (2023). Regional CO₂ inversion through ensemble-based simultaneous state and
 589 parameter estimation: TRACE framework and controlled experiments. *Journal*
 590 *of Advances in Modeling Earth Systems*, *15*(3), e2022MS003208.
- 591 Ciais, P., Reichstein, M., Viovy, N., Granier, A., Ogee, J., Allard, V., ... others
 592 (2005). Europe-wide reduction in primary productivity caused by the heat and
 593 drought in 2003. *Nature*, *437*(7058), 529–533. doi: [https://doi.org/10.1038/](https://doi.org/10.1038/nature03972)
 594 [nature03972](https://doi.org/10.1038/nature03972)
- 595 Davis, K. J., Browell, E. V., Feng, S., Lauvaux, T., Obland, M. D., Pal, S., ... oth-
 596 ers (2021). The atmospheric carbon and transport (act)-america mission.
 597 *Bulletin of the American Meteorological Society*, *102*(9), E1714–E1734.
- 598 Davis, K. J., Obland, M., Lin, B., Lauvaux, T., O’Dell, C., Meadows, B., ... Pauly,
 599 R. (2018). *ACT-America: L3 merged in situ atmospheric trace gases and*
 600 *flask data, eastern usa*. ORNL Distributed Active Archive Center. Retrieved
 601 from https://daac.ornl.gov/cgi-bin/dsviewer.pl?ds_id=1593 doi:
 602 10.3334/ORNLDAAAC/1593
- 603 DeLucia, E., Drake, J. E., Thomas, R. B., & Gonzalez-Meler, M. (2007). Forest
 604 carbon use efficiency: is respiration a constant fraction of gross primary pro-
 605 duction? *Glob. Change Biol.*, *13*(6), 1157–1167.
- 606 Fargione, J. E., Bassett, S., Boucher, T., Bridgham, S. D., Conant, R. T., Cook-
 607 Patton, S. C., ... others (2018). Natural climate solutions for the United
 608 States. *Science Advances*, *4*(11), eaat1869.
- 609 Feldman, A. F., Zhang, Z., Yoshida, Y., Chatterjee, A., & Poulter, B. (2023).
 610 Using Orbiting Carbon Observatory-2 (OCO-2) column CO₂ retrievals
 611 to rapidly detect and estimate biospheric surface carbon flux anoma-
 612 lies. *Atmospheric Chemistry and Physics*, *23*(2), 1545–1563. Retrieved
 613 from <https://acp.copernicus.org/articles/23/1545/2023/> doi:
 614 10.5194/acp-23-1545-2023
- 615 Feng, S., Lauvaux, T., Davis, K. J., Keller, K., Zhou, Y., Williams, C., ... Baker,
 616 I. (2019). Seasonal characteristics of model uncertainties from biogenic fluxes,
 617 transport, and large-scale boundary inflow in atmospheric CO₂ simulations
 618 over north america. *J. Geophys. Res.-Atmos.*, *124*(24), 14325–14346. doi:
 619 10.1029/2019JD031165
- 620 Feng, S., Lauvaux, T., Keller, K., Davis, K. J., Rayner, P., Oda, T., & Gurney,
 621 K. R. (2019). A road map for improving the treatment of uncertainties in
 622 high-resolution regional carbon flux inverse estimates. *Geophysical Research*
 623 *Letters*, *46*(22), 13461–13469.
- 624 Gelaro, R., McCarty, W., Suárez, M. J., Todling, R., Molod, A., Takacs, L., ...
 625 others (2017). The modern-era retrospective analysis for research and applica-

- 626 tions, version 2 (MERRA-2). *J. Climate*, *30*(14), 5419–5454.
- 627 Hall, B. D., Crotwell, A. M., Kitzis, D. R., Mefford, T., Miller, B. R., Schibig,
628 M. F., & Tans, P. P. (2021). Revision of the World Meteorological Or-
629 ganization Global Atmosphere Watch (WMO/GAW) CO₂ calibration
630 scale. *Atmospheric Measurement Techniques*, *14*(4), 3015–3032. Retrieved
631 from <https://amt.copernicus.org/articles/14/3015/2021/> doi:
632 10.5194/amt-14-3015-2021
- 633 He, L., Byrne, B., Yin, Y., Liu, J., & Frankenberg, C. (2022). Remote-sensing de-
634 rived trends in gross primary production explain increases in the CO₂ seasonal
635 cycle amplitude. *Global Biogeochemical Cycles*, *36*(9), e2021GB007220. doi:
636 10.1029/2021GB007220
- 637 He, W., Jiang, F., Ju, W., Byrne, B., Xiao, J., Nguyen, N. T., ... others (2023).
638 Do state-of-the-art atmospheric co2 inverse models capture drought impacts
639 on the european land carbon uptake? *Journal of Advances in Modeling Earth*
640 *Systems*, *15*(6), e2022MS003150.
- 641 He, Y., Piao, S., Li, X., Chen, A., & Qin, D. (2018). Global patterns of vege-
642 tation carbon use efficiency and their climate drivers deduced from MODIS
643 satellite data and process-based models. *Agricultural and Forest Meteorol-*
644 *ogy*, *256-257*, 150-158. Retrieved from [https://www.sciencedirect.com/](https://www.sciencedirect.com/science/article/pii/S0168192318300923)
645 [science/article/pii/S0168192318300923](https://www.sciencedirect.com/science/article/pii/S0168192318300923) doi: [https://doi.org/10.1016/](https://doi.org/10.1016/j.agrformet.2018.03.009)
646 [j.agrformet.2018.03.009](https://doi.org/10.1016/j.agrformet.2018.03.009)
- 647 Hu, L., Andrews, A. E., Thoning, K. W., Sweeney, C., Miller, J. B., Michalak,
648 A. M., ... van der Velde, I. R. (2019). Enhanced North American carbon
649 uptake associated with El Niño. *Science advances*, *5*(6), eaaw0076. doi:
650 10.1126/sciadv.aaw0076
- 651 Joiner, J., & Yoshida, Y. (2020). Satellite-based reflectances capture large fraction
652 of variability in global gross primary production (GPP) at weekly time scales.
653 *Agricultural and Forest Meteorology*, *291*, 108092. Retrieved from [https://](https://www.sciencedirect.com/science/article/pii/S0168192320301945)
654 www.sciencedirect.com/science/article/pii/S0168192320301945 doi:
655 <https://doi.org/10.1016/j.agrformet.2020.108092>
- 656 Joiner, J., & Yoshida, Y. (2021). *Global modis and fluxnet-derived daily gross pri-*
657 *mary production, v2*. ORNL DAAC, Oak Ridge, Tennessee, USA. doi: 10
658 .3334/ORNLDAAC/1835
- 659 Jung, M., Schwalm, C., Migliavacca, M., Walther, S., Camps-Valls, G., Koirala, S.,
660 ... Reichstein, M. (2020). Scaling carbon fluxes from eddy covariance sites to
661 globe: synthesis and evaluation of the FLUXCOM approach. *Biogeosciences*,
662 *17*(5), 1343–1365. Retrieved from [https://www.biogeosciences.net/17/](https://www.biogeosciences.net/17/1343/2020/)
663 [1343/2020/](https://www.biogeosciences.net/17/1343/2020/) doi: 10.5194/bg-17-1343-2020
- 664 Kim, J., Polavarapu, S. M., Jones, D. B., Chan, D., & Neish, M. (2021). The
665 resolvable scales of regional-scale co2 transport in the context of imperfect
666 meteorology: The predictability of co2 in a limited-area model. *Journal of*
667 *Geophysical Research: Atmospheres*, *126*(20), e2021JD034896.
- 668 Kirchmeier-Young, M. C., & Zhang, X. (2020). Human influence has intensified ex-
669 treme precipitation in North America. *Proceedings of the National Academy of*
670 *Sciences*, *117*(24), 13308-13313. Retrieved from [https://www.pnas.org/doi/](https://www.pnas.org/doi/abs/10.1073/pnas.1921628117)
671 [abs/10.1073/pnas.1921628117](https://www.pnas.org/doi/abs/10.1073/pnas.1921628117) doi: 10.1073/pnas.1921628117
- 672 Lauvaux, T., Schuh, A. E., Uliasz, M., Richardson, S., Miles, N., Andrews, A. E.,
673 ... Davis, K. J. (2012). Constraining the co₂ budget of the corn belt:
674 exploring uncertainties from the assumptions in a mesoscale inverse sys-
675 tem. *Atmospheric Chemistry and Physics*, *12*(1), 337–354. Retrieved
676 from <https://acp.copernicus.org/articles/12/337/2012/> doi:
677 10.5194/acp-12-337-2012
- 678 Li, X., & Xiao, J. (2019). Mapping photosynthesis solely from solar-induced chloro-
679 phyll fluorescence: A global, fine-resolution dataset of gross primary produc-
680 tion derived from OCO-2. *Remote Sensing*, *11*(21), 2563.

- 681 Li, X., Xiao, J., He, B., Altaf Arain, M., Beringer, J., Desai, A. R., . . . others
682 (2018). Solar-induced chlorophyll fluorescence is strongly correlated with
683 terrestrial photosynthesis for a wide variety of biomes: First global analysis
684 based on OCO-2 and flux tower observations. *Global change biology*, *24*(9),
685 3990–4008.
- 686 Liu, J., Bowman, K. W., & Henze, D. K. (2015). Source-receptor relationships
687 of column-average CO₂ and implications for the impact of observations
688 on flux inversions. *J. Geophys. Res.-Atmos.*, *120*(10), 5214–5236. doi:
689 10.1002/2014JD022914
- 690 Liu, J., Bowman, K. W., Schimel, D. S., Parazoo, N. C., Jiang, Z., Lee, M., . . .
691 Eldering, A. (2017). Contrasting carbon cycle responses of the tropical
692 continents to the 2015–2016 El Niño. *Science*, *358*(6360). Retrieved from
693 <http://science.sciencemag.org/content/358/6360/eam5690> doi:
694 10.1126/science.aam5690
- 695 Manzoni, S., Čapek, P., Porada, P., Thurner, M., Winterdahl, M., Beer, C., . . . Way,
696 D. (2018). Reviews and syntheses: Carbon use efficiency from organisms to
697 ecosystems – definitions, theories, and empirical evidence. *Biogeosciences*,
698 *15*(19), 5929–5949. Retrieved from [https://bg.copernicus.org/articles/](https://bg.copernicus.org/articles/15/5929/2018/)
699 [15/5929/2018/](https://bg.copernicus.org/articles/15/5929/2018/) doi: 10.5194/bg-15-5929-2018
- 700 Monteil, G., Broquet, G., Scholze, M., Lang, M., Karstens, U., Gerbig, C., . . . Wal-
701 ton, E. M. (2020). The regional european atmospheric transport inversion
702 comparison, eurocom: first results on european-wide terrestrial carbon fluxes
703 for the period 2006–2015. *Atmospheric Chemistry and Physics*, *20*(20), 12063–
704 12091. Retrieved from [https://acp.copernicus.org/articles/20/12063/](https://acp.copernicus.org/articles/20/12063/2020/)
705 [2020/](https://acp.copernicus.org/articles/20/12063/2020/) doi: 10.5194/acp-20-12063-2020
- 706 Munassar, S., Monteil, G., Scholze, M., Karstens, U., Rödenbeck, C., Koch, F.-T.,
707 . . . Gerbig, C. (2023). Why do inverse models disagree? a case study with
708 two european co₂ inversions. *Atmospheric Chemistry and Physics*, *23*(4),
709 2813–2828.
- 710 Munassar, S., Rödenbeck, C., Koch, F.-T., Totsche, K. U., Galkowski, M.,
711 Walther, S., & Gerbig, C. (2022). Net ecosystem exchange (nee) esti-
712 mates 2006–2019 over europe from a pre-operational ensemble-inversion
713 system. *Atmospheric Chemistry and Physics*, *22*(12), 7875–7892. Re-
714 trieved from <https://acp.copernicus.org/articles/22/7875/2022/> doi:
715 10.5194/acp-22-7875-2022
- 716 NOAA. (2021, July). *ETOPO 2022 15 Arc-Second Global Relief Model*. NOAA
717 National Centers for Environmental Information. Retrieved from [https://doi](https://doi.org/10.25921/fd45-gt74)
718 [.org/10.25921/fd45-gt74](https://doi.org/10.25921/fd45-gt74) doi: 10.25921/fd45-gt74
- 719 O'Dell, C. W., Eldering, A., Wennberg, P. O., Crisp, D., Gunson, M. R., Fisher, B.,
720 . . . Velasco, V. A. (2018). Improved retrievals of carbon dioxide from orbiting
721 carbon observatory-2 with the version 8 acos algorithm. *Atmos. Meas. Tech.*,
722 *11*(12), 6539–6576. Retrieved from [https://www.atmos-meas-tech.net/11/](https://www.atmos-meas-tech.net/11/6539/2018/)
723 [6539/2018/](https://www.atmos-meas-tech.net/11/6539/2018/) doi: 10.5194/amt-11-6539-2018
- 724 Ogle, S. M., Davis, K., Lauvaux, T., Schuh, A., Cooley, D., West, T. O., . . . Den-
725 ning, A. S. (2015, mar). An approach for verifying biogenic greenhouse gas
726 emissions inventories with atmospheric CO₂ concentration data. *Environmental*
727 *Research Letters*, *10*(3), 034012. Retrieved from [https://dx.doi.org/](https://dx.doi.org/10.1088/1748-9326/10/3/034012)
728 [10.1088/1748-9326/10/3/034012](https://dx.doi.org/10.1088/1748-9326/10/3/034012) doi: 10.1088/1748-9326/10/3/034012
- 729 Schuldt, K. N., Mund, J., Luijkx, I. T., Aalto, T., Abshire, J. B., Aikin, K., . . .
730 van den Bulk, P. (2022). *Multi-laboratory compilation of atmospheric carbon*
731 *dioxide data for the period 1957-2021; obspack_co2_1_globalviewplus_v8.0_2022-*
732 *08-27*. NOAA Global Monitoring Laboratory. doi: 10.25925/20220808
- 733 Seneviratne, S., Zhang, X., Adnan, M., Badi, W., Dereczynski, C., Di Luca, A., . . .
734 Zhou, B. (2021). [Book Section]. In V. Masson-Delmotte et al. (Eds.), *Climate*
735 *change 2021: The physical science basis. contribution of working group i to*

- 736 *the sixth assessment report of the intergovernmental panel on climate change*
737 (chap. Weather and Climate Extreme Events in a Changing Climate). Cam-
738 bridge University Press, Cambridge, United Kingdom and New York, NY,
739 USA: Cambridge University Press. doi: 10.1017/9781009157896.013
- 740 Shenoy, S., Gorinevsky, D., Trenberth, K. E., & Chu, S. (2022). Trends of
741 extreme US weather events in the changing climate. *Proceedings of the*
742 *National Academy of Sciences*, 119(47), e2207536119. Retrieved from
743 <https://www.pnas.org/doi/abs/10.1073/pnas.2207536119> doi:
744 10.1073/pnas.2207536119
- 745 Stanevich, I., Jones, D. B. A., Strong, K., Parker, R. J., Boesch, H., Wunch, D., ...
746 Deng, F. (2020). Characterizing model errors in chemical transport mod-
747 eling of methane: impact of model resolution in versions v9-02 of geos-chem
748 and v35j of its adjoint model. *Geosci. Model Dev.*, 13(9), 3839–3862. Re-
749 trieved from <https://gmd.copernicus.org/articles/13/3839/2020/> doi:
750 10.5194/gmd-13-3839-2020
- 751 Sun, Q., Zhang, X., Zwiers, F., Westra, S., & Alexander, L. V. (2021). A
752 global, continental, and regional analysis of changes in extreme precipi-
753 tation. *Journal of Climate*, 34(1), 243 - 258. Retrieved from [https://](https://journals.ametsoc.org/view/journals/clim/34/1/jcliD190892.xml)
754 journals.ametsoc.org/view/journals/clim/34/1/jcliD190892.xml doi:
755 10.1175/JCLI-D-19-0892.1
- 756 Sun, Y., Frankenberg, C., Wood, J. D., Schimel, D., Jung, M., Guanter, L., ...
757 others (2017). OCO-2 advances photosynthesis observation from space via
758 solar-induced chlorophyll fluorescence. *Science*, 358(6360), eaam5747.
- 759 Thompson, R. L., Broquet, G., Gerbig, C., Koch, T., Lang, M., Monteil, G., ... oth-
760 ers (2020). Changes in net ecosystem exchange over europe during the 2018
761 drought based on atmospheric observations. *Philosophical Transactions of the*
762 *Royal Society B*, 375(1810), 20190512.
- 763 Turner, A. J., Köhler, P., Magney, T. S., Frankenberg, C., Fung, I., & Cohen,
764 R. C. (2021). Extreme events driving year-to-year differences in gross pri-
765 mary productivity across the us. *Biogeosciences*, 18(24), 6579–6588. Re-
766 trieved from <https://bg.copernicus.org/articles/18/6579/2021/> doi:
767 10.5194/bg-18-6579-2021
- 768 U.S. Energy Information Administration. (2023). *Energy-related CO₂ emission data*
769 *tables*. <https://www.eia.gov/environment/emissions/state/>. (Accessed 11
770 Aug 2023)
- 771 USDA-NASS. (2020). *Nass - quick stats*. USDA National Agricultural Statistics Ser-
772 vice. Washington DC.
- 773 van der Werf, G. R., Randerson, J. T., Giglio, L., van Leeuwen, T. T., Chen,
774 Y., Rogers, B. M., ... Kasibhatla, P. S. (2017). Global fire emissions
775 estimates during 1997–2016. *Earth Syst. Sci. Data*, 9(2), 697–720. Re-
776 trieved from <https://www.earth-syst-sci-data.net/9/697/2017/> doi:
777 10.5194/essd-9-697-2017
- 778 Wei, Y., Shrestha, R., Pal, S., Gerken, T., Feng, S., McNelis, J., ... others (2021).
779 Atmospheric Carbon and Transport–America (ACT-America) data sets:
780 Description, management, and delivery. *Earth and Space Science*, 8(7),
781 e2020EA001634. doi: 10.1029/2020EA001634
- 782 West, T. O., Bandaru, V., Brandt, C. C., Schuh, A. E., & Ogle, S. M. (2011). Re-
783 gional uptake and release of crop carbon in the united states. *Biogeosciences*,
784 8(8), 2037–2046. Retrieved from [https://bg.copernicus.org/articles/8/](https://bg.copernicus.org/articles/8/2037/2011/)
785 [2037/2011/](https://bg.copernicus.org/articles/8/2037/2011/) doi: 10.5194/bg-8-2037-2011
- 786 West, T. O., Brandt, C. C., Baskaran, L. M., Hellwinckel, C. M., Mueller, R.,
787 Bernacchi, C. J., ... others (2010). Cropland carbon fluxes in the united
788 states: Increasing geospatial resolution of inventory-based carbon accounting.
789 *Ecological Applications*, 20(4), 1074–1086.

- 790 Yin, Y., Byrne, B., Liu, J., Wennberg, P. O., Davis, K. J., Magney, T., . . . others
791 (2020). Cropland carbon uptake delayed and reduced by 2019 midwest floods.
792 *AGU Advances*, 1(1), e2019AV000140.
- 793 Yu, K., Keller, C. A., Jacob, D. J., Molod, A. M., Eastham, S. D., & Long, M. S.
794 (2018). Errors and improvements in the use of archived meteorological
795 data for chemical transport modeling: an analysis using GEOS-Chem v11-
796 01 driven by GEOS-5 meteorology. *Geosci. Model Dev.*, 11(1), 305–319.
797 Retrieved from <https://www.geosci-model-dev.net/11/305/2018/> doi:
798 10.5194/gmd-11-305-2018
- 799 Yu, S., Falco, N., Patel, N., Wu, Y., & Wainwright, H. (2023, jun). Diverging cli-
800 mate response of corn yield and carbon use efficiency across the U.S. *Environ-*
801 *mental Research Letters*, 18(6), 064049. Retrieved from [https://dx.doi.org/](https://dx.doi.org/10.1088/1748-9326/acd5e4)
802 [10.1088/1748-9326/acd5e4](https://dx.doi.org/10.1088/1748-9326/acd5e4) doi: 10.1088/1748-9326/acd5e4
- 803 Zscheischler, J., Westra, S., Hurk, B. J. J. M. v. d., Seneviratne, S. I., Ward, P. J.,
804 Pitman, A., . . . Zhang, X. (2018). Future climate risk from compound events.
805 *Nature Climate Change*, 8(6), 469–477.